

Article

# Vibration Analysis of the Third Rail Structure of a Mass Rapid Transit System with Structural Defects

Milan Paudel <sup>1,2,\*</sup>, Li Jie Lim <sup>1,2</sup>, Fook Fah Yap <sup>1,2</sup> and Kevin Kho <sup>2</sup>

<sup>1</sup> School of Mechanical and Aerospace Engineering, Nanyang Technological University, 50 Nanyang Avenue, Singapore 639798, Singapore; m170049@e.ntu.edu.sg (L.J.L.); mffyap@ntu.edu.sg (F.F.Y.)

<sup>2</sup> SMRT-NTU Urban Rail Corporate Laboratory, 50 Nanyang Avenue, Singapore 639798, Singapore; kevin.kho@smrt.com.sg

\* Correspondence: milan002@e.ntu.edu.sg

**Featured Application:** The work presented in this manuscript can be used as a reference for predicting the possible structural damage or failure in the third rail structures.

**Abstract:** The third rail is a critical piece of railway infrastructure that provides a continuous supply of electricity to power mass rapid transit trains. The vibration of the third rail may excite different resonant modes and affect its structural integrity and reliability by degrading the mechanical properties leading to the damaged or missing structural components. This paper examines vibrational characteristics of the third rail of Singapore Mass Rapid Transit system with damaged and missing structural components. Using the mathematical model, the first five, pin-to-pin modes of vibration and natural frequencies were identified and compared with modal and harmonic response obtained from ANSYS finite element models. A good agreement was observed between the analytical and numerical solutions. The study was further extended to study the sagging of the third rail due to structural failure and its impact on collector shoes. It was found that the structural defects could produce resonance modes below 5 Hz. In addition, the sagging and contact force on collector shoes increased by multiple folds when more than 2 claw structures are broken. The methods and the results presented in this article can be used as a tool for predictive maintenance by detecting possible structural failure or defects.

**Keywords:** third rail vibration; conductor rail; Euler–Bernoulli beam; periodically supported beam; mobility analysis; third rail deflection; pin-to-pin resonance



**Citation:** Paudel, M.; Lim, L.J.; Yap, F.F.; Kho, K. Vibration Analysis of the Third Rail Structure of a Mass Rapid Transit System with Structural Defects. *Appl. Sci.* **2021**, *11*, 8410. <https://doi.org/10.3390/app11188410>

Academic Editor: Araliya Mosleh

Received: 22 August 2021

Accepted: 7 September 2021

Published: 10 September 2021

**Publisher's Note:** MDPI stays neutral with regard to jurisdictional claims in published maps and institutional affiliations.



**Copyright:** © 2021 by the authors. Licensee MDPI, Basel, Switzerland. This article is an open access article distributed under the terms and conditions of the Creative Commons Attribution (CC BY) license (<https://creativecommons.org/licenses/by/4.0/>).

## 1. Introduction

Train and railway networks are among the most critical infrastructures for modern transportation and development. Millions of commuters depend on the mass transit system for daily transportation. In Singapore, more than 2.2 million people use mass rapid transit (MRT) daily. Most of the modern trains run on electricity, and uninterrupted operation demands a continuous supply of electric power. There are two major electrification systems adopted in urban railway. The first is the overhead system, and the second is the third rail system [1]. The third rail, also known as the conductor rail, is the most commonly used method to drive the trains in modern mass transit systems and is considered more efficient and economical compared with the overhead systems [2]. The third rail is usually placed on the sleeper's ends on the railway trackside and runs parallel to the railway track, as shown in Figure 1. It is supplied with DC electricity.

The earliest third rails were made of steel [3]. The second type of the third rail is known as 84C, where rivets are used to bond the aluminum to the web of steel rail. The third and the most recent type is the Aluminum/Stainless Steel (ALSS) rail, where stainless steel is attached to the aluminum [3]. The trains have contact blocks, called current collector shoes or contact shoes, which remain in contact with the third rail and draw the necessary

DC electric traction power to drive the train [4]. There are three different positions at which collector shoes make contact with the third rail, as shown in Figure 1. Some of the earliest systems used the top contact position. However, top contact systems are prone to environmental conditions such as rain, snow, and frost [5]. The more recent third rail system adopted a side contact or bottom contact system that allows the third rail to be covered for better environmental protection and safety, as used in Singapore.

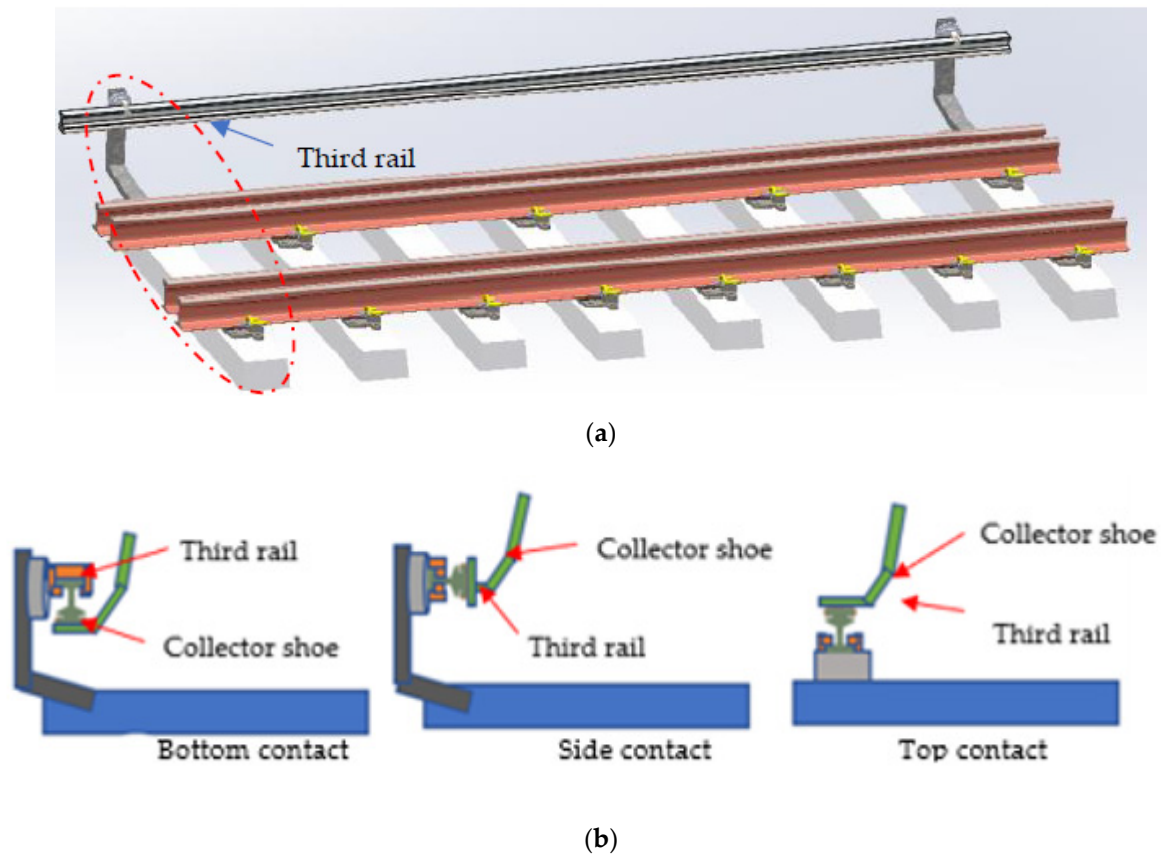


**Figure 1.** (a) Third rail setup and (b) types of collector shoe and third rail contact arrangements.

The third rail is an important component of the railway system. It is well known that higher train speed increases the vibration of the ground [6] and railway tracks [7]. Similarly, the third rail is also subject to increased vibration due to higher train speed [8]. Intense vibration in the third rail may excite resonance modes of the third rail and may reduce the supporting structure's service life, including insulator, bracket, and the third rail joints. The vibration deflection of the rail between the supports could also adversely impact the proper transmission of current to the collector shoes and must be properly understood and accounted for in the system design [3]. Therefore, it is essential to evaluate the structural characteristics of the third rail to better understand potential failure scenarios and predictive maintenance.

Much research has been conducted on the dynamics of railway tracks system. One of the basic approaches is to consider the track to be of infinite length. The railway tracks are often represented by Euler–Bernoulli beams or Timoshenko beams. The basic railway track model assumes an infinite beam on a continuous elastic Winkler foundation [9]. Further improvements include beam on a two-layer support model to account for the resilient rail pads between the rail and the sleeper and the ballast, beam on discrete support model, and so on [10–12]. Such analytical approaches, as well as the finite element approaches [13,14] using software such as ANSYS and ABAQUS, have been successfully used for parametric study and to understand the vibration characteristics of the railway track.

However, most of the third rail systems research is focused on the electrical system configuration [13], shoe-gear dynamics, and overhead conductor rails [14,15]. Weston [16] studied the displacement of the electric shoe-gears and contact force. Vera et al. [14] used a simulation technique to design a new overhead conductor rail. Jinfa et al. [8] studied the dynamics of combined electric shoe-gear and conductor rail by simplifying the electric shoe-gear and conductor rail system as a cantilever with a rotating mechanism attached to a simply supported Euler–Bernoulli beam. Nonetheless, there has not been much research to identify the different modes of vibration and frequencies at which they occur. Most importantly, the authors could not find any research that studies the vibrational characteristics of the third rail with missing, damaged, or degraded structural components. On the other hand, existing analyses on the third rail are often limited to single-span length. A more realistic model would be to represent the third rail to be of infinite length. Furthermore, the third rail model can be improved by treating it as a beam on periodic springs with certain stiffness to represent the supporting structure. Such a model can be used to obtain different resonance frequencies and modes of vibration to evaluate the third rail vibration dynamics. The model can be easily extended to study the effect of structural failure on the vibrational characteristics of the third rail, which can be useful for the predictive maintenance.

In this paper, the vertical vibration characteristics of the third rail structure of Singapore Mass Rapid Transit (SMRT) system were analyzed. First, a single-span Finite-Element Model was developed based on the design parameters of SMRT, and the results were validated against the single-span third rail setup in NTU-SMRT lab. After experimental verification of the FE model, the model was extended to multi-span third rail model. Moreover, the third rail was analytically modelled by considering an infinite beam on periodic spring supports. The mode shapes and corresponding natural frequencies were obtained from mathematical model and compared with the ANSYS finite element modal analysis results. An emphasis was given to understand the effect of different structural failure scenarios on vibration dynamics for predictive maintenance. The analysis was further extended to include the third rail deflection due to structural failure such as missing claws or deterioration in the support structure.

## 2. Finite Element Model Development

SMRT uses a bottom-contact third rail system, with the third rail being ALSS type. The typical third rail arrangement is shown in Figure 2a,b. The structural properties of each component in the support structure and the third rail are listed in Table 1.

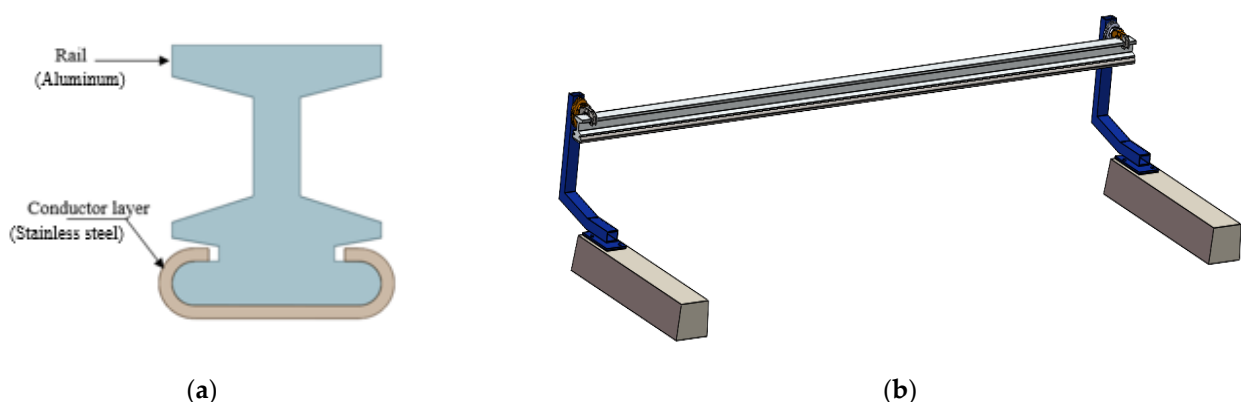
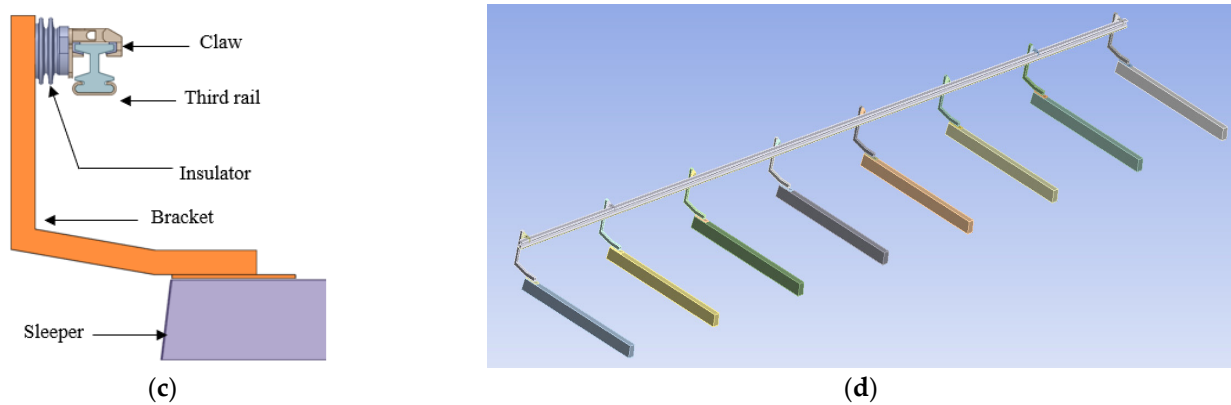


Figure 2. Cont.



**Figure 2.** Finite element model of third rail system: (a) conductor rail model; (b) typical third rail arrangement, (c) single-span third rail model; and (d) multi-span third rail model.

**Table 1.** Material properties of SMRT third rail components \*.

	Aluminum Rail	Conductor Rail	Bracket	Sleeper	Fasteners
Material	Aluminum alloy 6063	Stainless steel 430	Structural steel	Concrete	Stainless Steel 316
Density (kg/m <sup>3</sup> )	2700	7740	7850	2300	8027
Shear modulus (Pa)	2.59 × 10 <sup>10</sup>	7.84 × 10 <sup>10</sup>	7.69 × 10 <sup>10</sup>	1.27 × 10 <sup>10</sup>	8.2 × 10 <sup>10</sup>
Young’s modulus (Pa)	6.89 × 10 <sup>10</sup>	2 × 10 <sup>11</sup>	2 × 10 <sup>11</sup>	-	2 × 10 <sup>11</sup>
Cross-sectional area (m <sup>2</sup> )	4.70 × 10 <sup>-3</sup>	6.59 × 10 <sup>-4</sup>	-	-	-

\* Values are based on third rail used in SMRT.

A detailed 3D model of a single-span third rail was developed based on the available dimensional information and material properties, as shown in Figure 2c. The single-span third rail model was validated against ANSYS finite element analysis and experimental modal testing. The validated single-span third rail model was then extended to a multi-span third rail model, as shown in Figure 2d. The multi-span model consists of a 35 m long rail, which is supported by eight supporting structures. The distance between two consecutive support structures is maintained at 4.9 m, as per the SMRT standard. As mentioned earlier, the supporting structures were replaced by spring arrangements with equivalent stiffness to simplify the model further. The contact between aluminum rail and stainless-steel conductor rail was defined as bonded. A default meshing in Workbench Mechanical was applied, which included element types such as Solid186, CONTA174, Beam188, and COMBIN 14. The element size was selected to be 0.1 m, which resulted in the number of nodes and elements to be 121,004 and 24,546, respectively.

The equivalent stiffness of the support structures depends on the material and design. Based on the published articles, typical stiffness values for third rail support structures might range from 0.1 MN/m to 20 MN/m [8,17]. Based on the material properties and design of the SMRT support structure, the equivalent spring stiffness for the supporting structures in three different directions, namely vertical, lateral, and longitudinal, were estimated to be 2.4 MN/m, 0.86 MN/m and 0.8 MN/m, respectively, by applying a known force at the bracket and simulating the structural deflection.

### 3. Mathematical Model

The rail structure is well represented by an Euler–Bernoulli beam of infinite length on periodic spring supports [10,17]. The equation of free motion of an unsupported Euler–Bernoulli beam excited by a point harmonic force in the absence of damping is given by [18]:

$$EI \frac{\partial^4 y}{\partial x^4} + m_r' \frac{\partial^2 y}{\partial t^2} = F e^{i\omega t} \delta(x) \tag{1}$$

where  $E$  is the combined effective Young’s modulus of the third rail,  $I$  is the second moment of inertia, and  $EI$  is collectively known as bending stiffness of the beam.  $m'_r$  is the mass per unit length of the beam,  $y(x, t)$  is the vertical displacement/bending of the beam,  $x$  is the coordinate along the rail, and  $Fe^{i\omega t}$  represents the harmonic force with frequency  $\omega$  rad/s. The combined effective Young’s modulus of the third rail was estimated by using the material properties of the aluminum rail and stainless-steel conductor layer using Equation (2) [19].

$$\text{Effective Young's modulus } (E) = \frac{E_{AL}A_{AL} + E_{SS}A_{SS}}{A_{AL} + A_{SS}} \tag{2}$$

where  $E_{AL}, E_{SS}, A_{AL}$  and  $A_{SS}$  are Young’s moduli and the cross-sectional areas of the aluminum rail and stainless-steel conductor, respectively.

The free wave solution of Equation (1) considering the harmonic motion of frequency  $\omega$  rad/s is given by:

$$y(x, t) = Ue^{i\omega t}e^{-kx} \tag{3}$$

where  $U$  is the amplitude coefficient, and  $k$  is the wavenumber. Substituting Equation (3) in Equation (1), the wavenumbers of the unsupported beam is given by:

$$k = \left( \frac{m'_r\omega^2}{EI} \right)^{\frac{1}{4}} \tag{4}$$

Moreover, the third rail can be modelled as an infinite beam that is periodically supported by springs separated by a distance  $d$  [8,17,20], as illustrated in Figure 3. Analysis for the periodically supported beam is also described in [10,18,21]. A general approach is to account for the reaction forces at each support point that is exerted by individual deflected springs on the beam. If the deflection/bending of the beam at the support point  $x_n = nd$  is  $u(x_n)$ , the beam experiences a reaction force equivalent to  $-Ku(x_n)$ , where  $K$  is the stiffness of the supporting springs. The procedure to estimate the equivalent spring stiffness for the third rail support structure was explained in Section 2.

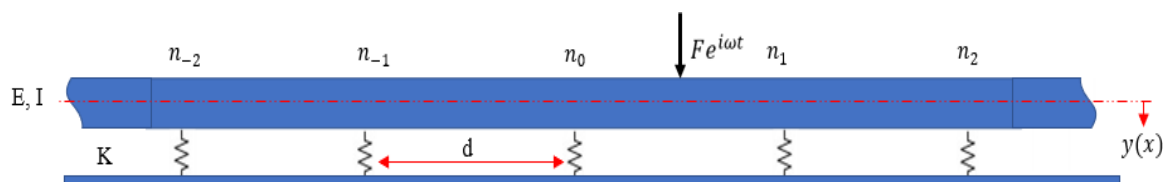


Figure 3. Illustration of the equivalent mathematical model for analytical solution.

In general, the dynamics of the periodically supported structure is analyzed using a receptance function  $\alpha(x, x')$  defined as the dynamic response of each structure under unit force excitation [12]. The receptance function for the Euler–Bernoulli beam is given by [10]:

$$\alpha(x, x') = u_1e^{-ik_e|x-x'|} + u_2e^{-ik_p|x-x'|} \tag{5}$$

where  $k_e$  and  $k_p$  are the wavenumbers, which are the negative imaginary and positive real solutions of Equation (4). As explained in [10], the coefficients  $u_1$  and  $u_2$  are given by:

$$u_1 = \frac{-i}{4EI k_e^3}, \text{ and } u_2 = \frac{-i}{4EI k_p^3} \tag{6}$$

Finally, the total response of the beam at any position  $x$  along the beam to a harmonic point force applied at  $x_c$ , such that  $0 \leq x_c \leq d$ , is given by:

$$y(x) = F \alpha(x, x_c) - K \sum_{n=-\infty}^{\infty} \alpha(x, x_n) y(x_n) \quad (7)$$

Equation (7) can be used to calculate the deflection of the beam  $y(x_m)$  at each support  $x_m$  as:

$$y(x_m) = F \alpha(x_m, x_c) - K \sum_{n=-N}^N \alpha(x_m, x_n) y(x_n) \quad (8)$$

Here, the infinite length of the third rail was truncated to  $n = -N$  to  $N$ . Thus, the total number of supports considered is equal to  $2N + 1$ . It should be noted that the support point  $x_m$  represents particular support of interest among many supporting springs at a distance  $x_n = nd$ . Equation (8) can be rearranged into matrix form and solved for  $y(x_n)$ . Thereafter, the deflection at each support point can be used to obtain the total response of the beam as:

$$y(x) = F \alpha(x, x_c) - K \sum_{n=-N}^N \alpha(x, x_n) y(x_n) \quad (9)$$

Furthermore, the force response to a point harmonic force can be analyzed in terms of mobility analysis. The mobility is defined in terms of the dynamic force acting at a point and the response in terms of velocity [20]. Mobility is a frequency-dependent quantity and is often regarded as a frequency response. It gives the magnitude and phase relationship between the excitation force and the response. The mobility of the beam for a unit harmonic force can be calculated as:

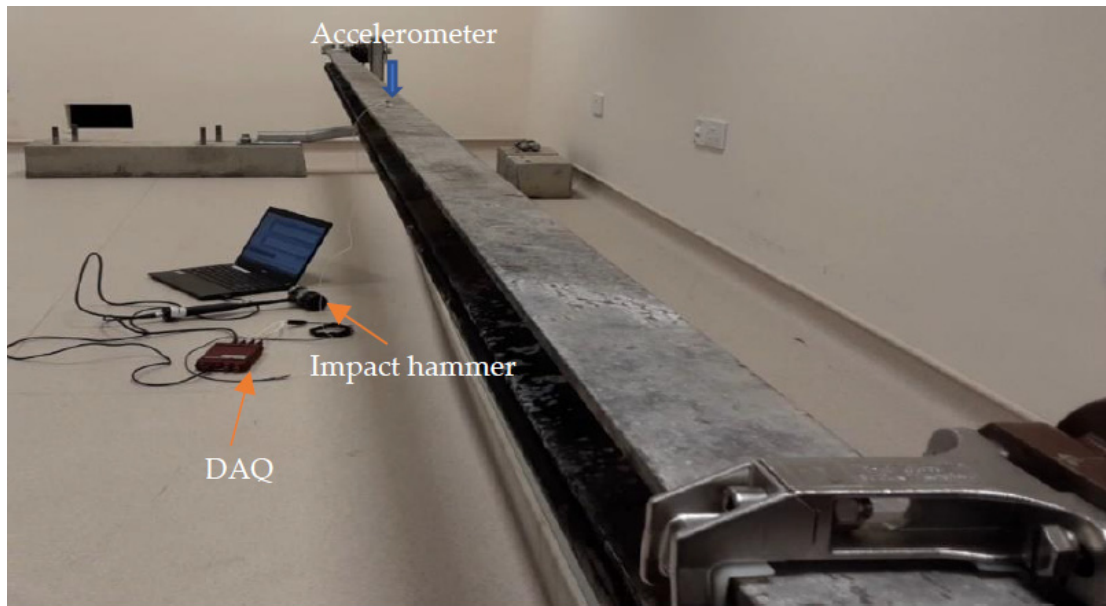
$$\text{Mobility}(Y) = i * \omega * y(x) \quad (10)$$

## 4. Results and Discussion

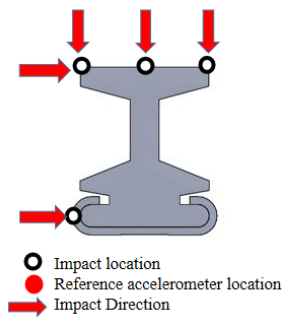
### 4.1. Experimental Validation of the FEM Model

A single-span third rail setup was developed at the NTU-SMRT Urban Rail Corporate Laboratory. The main objective of conducting the experimental analysis is to validate the third rail's Finite Element Model.

A roving hammer impact approach is adopted for laboratory modal testing of the third rail. The third rail is impacted at different locations using an impact hammer while keeping the accelerometer sensor's position fixed. The length of the third rail was divided into 11 sections. For each section, the third rail is impacted at five different locations. The laboratory setup of SMRT third rail, impact locations, accelerometer position, and direction of impact is shown in Figure 4a. The SignalCalc [21] analyzer was used to acquire the data from the accelerometer and the impact hammer. Thereafter, MEScopeVES [22] software was used to further process the data. The experimental procedure has a few steps including collection of frequency response functions (FRFs) by striking the hammer at selected impact locations along the rail and aggregating the complete dataset into the analysis software, MEScopeVES. Impact hammer strikes act as an excitation input to the structure, and the response in time domain is captured using an accelerometer. The captured data are then converted into frequency domain [23]. A dataset of 54 FRFs was collected in this experiment. The dataset was then used in MEScopeVES software along with a CAD model of the structure. MEScopeVES software analyses the imaginary part of the FRF to extract the amplitude and direction of the response. Moreover, the software also extracts parameters such as frequency and damping [24,25]. The software then combines the CAD model of the structure and extracted modal parameters to visually present mode shapes. In this way, the mode shapes and corresponding frequencies were obtained for the single-span third rail using the experimental data.

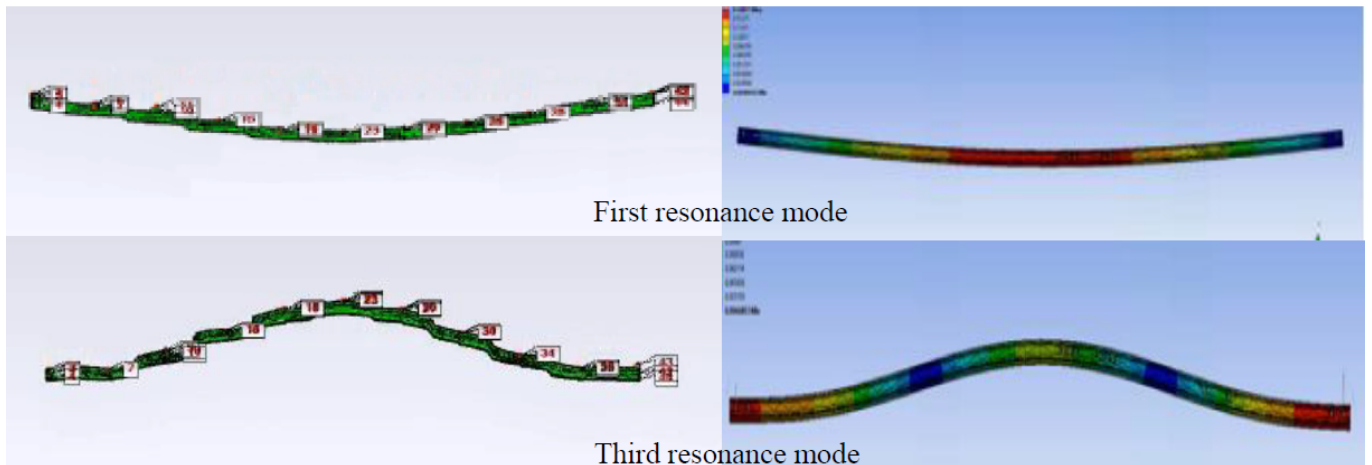


(a)



(b)

Experimental analysis



(c)

**Figure 4.** (a) Experimental set-up for modal testing; (b) impact points' locations on third rail set up for roving hammer test; (c) comparison between the mode shapes obtained from experimental and FEM analysis.

The experimental modal testing results are compared with the results obtained from numerical analysis using ANSYS for the single-span Finite Element Model. Figure 4b shows the typical examples of mode shapes obtained from experimental and FEM analysis.

Furthermore, Table 2 presents the natural frequencies corresponding to the first five modes. The first three modes were identified accurately, with the difference between experimental and FEM results of less than 5%. The discrepancy between the FEM and experimental results increases for higher modes. The higher modes are very sensitive to small imperfections and boundary conditions; therefore, it is common to have greater discrepancies for the higher modes of vibration. The results show a good agreement between the experiment and the FEM analysis. We conclude that the FEM model and the approach used to analyze the vibration analysis give acceptable results.

**Table 2.** Natural frequencies for first five modes of vibration obtained from experimental and FEM analysis.

Mode	Resonance Frequencies (Hz)		Difference (%)
	Experimental	FEM	
1	11.3	11.15	1.35
2	38.8	38.77	0.07
3	67.5	69.84	3.35
4	91.3	101.7	10.2
5	128.0	150.36	14.9

#### 4.2. Analysis of Multi-Span Third Rail Model

Building on the experimental verification of the finite element model, the analysis was extended to a 35 m multi-span third rail. Here, the results from the validated finite element model for multi-span third rail were compared against the results from the mathematical model developed in Section 3. The parameters listed in Table 3 for SMRT third rail were used to calculate the analytical solution for Equations (9) and (10).

**Table 3.** Equivalent structural parameters for analytical solution.

Parameters	Units	Values
Effective Young's modulus ( $E$ )	N/m <sup>2</sup>	$8.485 \times 10^{10}$
Second moment of inertia ( $I$ )	m <sup>4</sup>	$6.45 \times 10^{-6}$
Distance between two supports ( $d$ )	m	4.9
Mass per unit length of beam ( $m'_r$ )	Kg/m	17.8025
Equivalent spring stiffness of the support ( $K$ )	MN/m	2.4

Figure 5a compares the numerical solution for the spring-supported multi-span third rail model and the analytical solution of the mathematical model. The analytical solution is for the point mobility of the third rail due to a unit harmonic force at mid-span, i.e.,  $x_c = d/2$ . It should be noted that no damping properties of either the third rail or the supporting structures/springs were considered in this analysis.

The major difference between assuming continuous support and discrete periodic support is the presence of pin-to-pin vibration modes. Here, pins represent the discrete spring support points. Pin-to-pin vibration resonance occurs at specific frequencies when the wavelength of the vibration propagation is comparable to the distance between the two supports,  $d$ . Pin-to-pin vibration resonance appears in one basic mode (first mode) and several higher modes [26]. The first pin-to-pin vibration occurs when the wavelength of the propagation is double the distance between two supports. Similarly, the second pin-to-pin vibration occurs when the wavelength is equal to the distance between two supports, and so on.

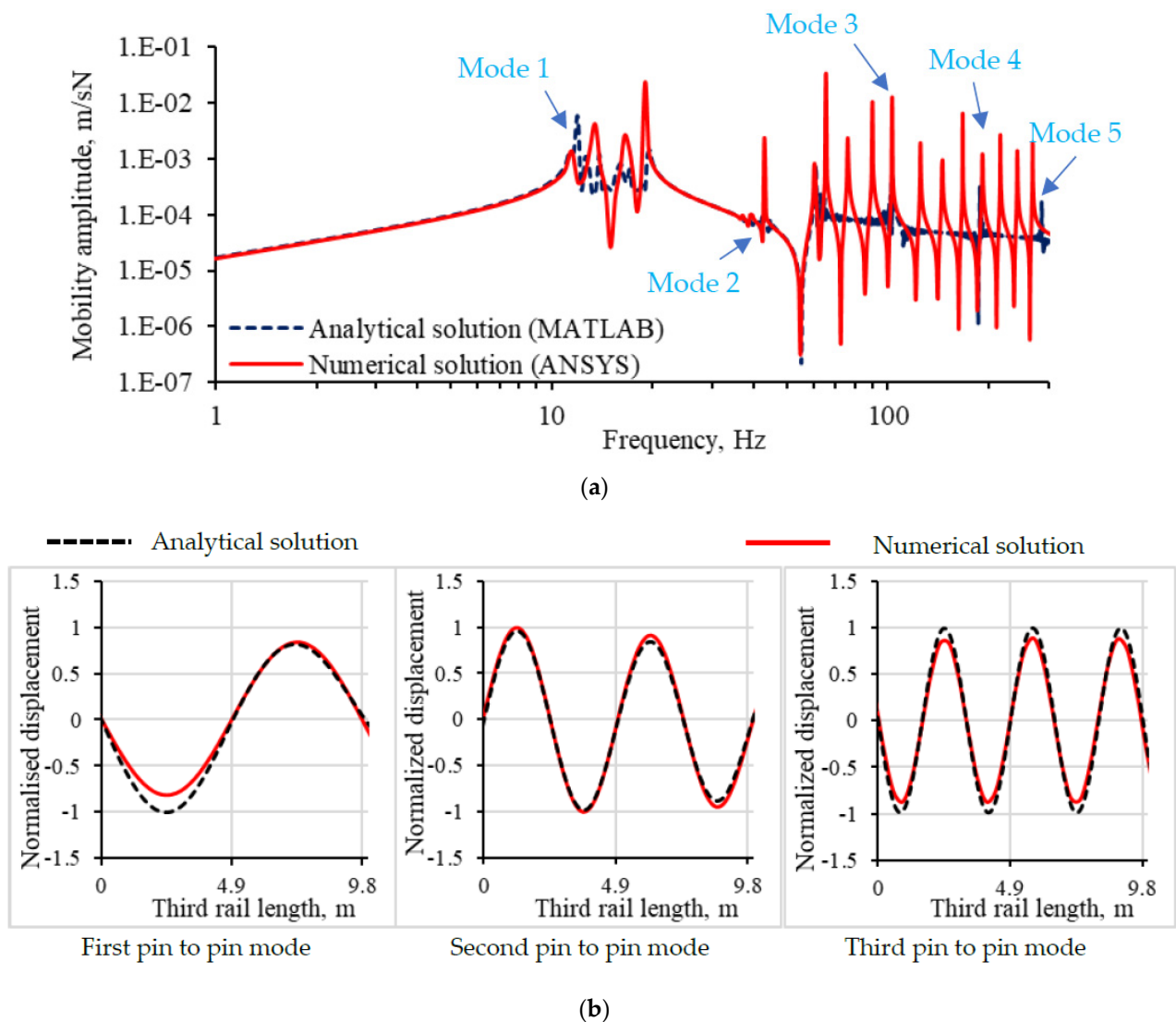


**Figure 5.** Analysis of multi-span third rail structure using analytical and numerical approaches; (a) mobility analysis of multi-span third rail: excited at mid span; (b) pin-to-pin resonance mode of vibrations.

The peaks of the mobility magnitude vs. frequency graph show vibration resonance of different modes. It is interesting to note that the first five pin-to-pin modes of vibration for the third rail occur below 300 Hz compared with the typical first pin-to-pin mode for railway structure, which occurs above 1000 Hz [10]. For SMRT third rail parameters, the first or basic pin-to-pin mode was found at 11.94 Hz based on the analytical solution. Similarly, the numerical solution from ANSYS simulation predicts the same mode at 11.74 Hz. A lower bending stiffness, lower mass per unit length, and a longer span length between supports are the reasons for the low pin-to-pin resonant frequency. It should also be noted that, while the mobility amplitude from the mathematical model mostly shows pin-to-pin modes, the ANSYS simulation includes many other non-pin-to-pin modes of vibration, especially at frequencies above 100 Hz. Although an FEM analysis gives more mode shapes compared with the analytical approach, it requires considerable computation time. As such, it is more convenient to use an analytical model for performing parametric analysis to analyze different scenarios such as the effect of a change in third rail material properties, structural parameters, and so on. An accurate analytical model can be used for a quick analysis of a given third rail system and structural properties. Therefore, in this study, the analytical model is compared with the FEM analysis to check for accuracy.

Thereafter, the analytical model was extended to analyze the effect of parameter changes due to structural deterioration.

Figure 5b presents the mode shapes of the first three pin-to-pin modes obtained from both analytical solution and Ansys simulation. A two-span length of the third rail was shown to illustrate the mode shapes. In ANSYS modal analysis, the displacement of the beam is arbitrarily scaled. Therefore, the results from both the analytical and numerical solution are normalized by the maximum value. The results show how a point will be deflected or displaced relative to another.

Table 4 shows the comparison between the frequencies of the first five pin-to-pin modes of vibration from the analytical and numerical solution. A good agreement was obtained for the pin-to-pin the mode of resonance vibration from both the analytical and numerical approaches. The difference between the analytical and numerical solution was found to be less than 6%.

**Table 4.** Resonance frequencies for the pin-to-pin modes of vibration obtained from both analytical and numerical approach.

Pin to Pin Mode	Analytical Solution (Hz)	Numerical Solution (Hz)	% Difference
1	11.94	11.74	1.7
2	46.72	44.93	4.0
3	103.29	103.02	0.2
4	183.19	176.83	3.4
5	286.32	269.36	6.1

#### 4.3. Analysis with Damaged Structural Components

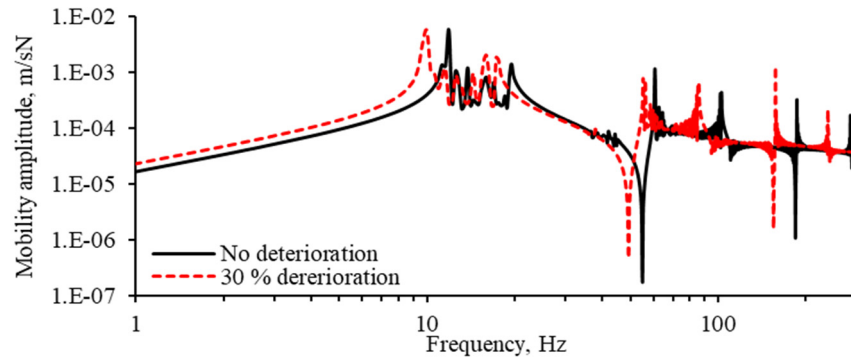
Strong vibration of the third rail can deteriorate and even cause the failure of the third rail structural components. It is essential to understand the characteristics of structural damage for predictive maintenance. Although the third rail is subjected to the moving load applied by the collector shoe on the third rail, from the conditional monitoring aspect, the operators often perform tests on railway tracks during off-hours when the trains are not operating. A roving hammer test by applying stationary load at different locations on the third rail helps to monitor if the structural integrity has been compromised due to prolong resonant vibration. This section presents the effect of structural deterioration of components on the vibrational behavior of the third rail.

##### 4.3.1. The Effect of Structural Deterioration

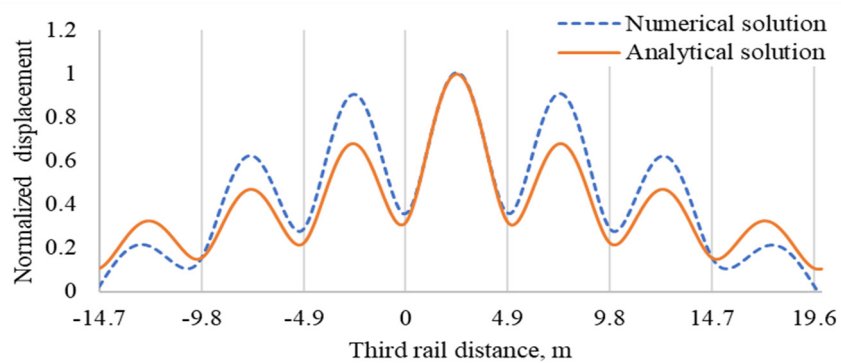
Strong railway vibrations could produce damaging effects on structural components of the rail [11]. Similarly, the third rail resonant vibrations can easily degrade the third rail and its components such as brackets, insulators, or claws over time [17]. Such vibration-induced damages can cause fatigue failure and greater wear and tear, as well as reducing the stiffness of the third rail and the supporting structures [27]. Mathematically, it can be modeled by reducing the bending stiffness ( $EI$ ) for the third rail and the spring stiffness ( $K$ ) for the support structures. An effect of structural deterioration on its dynamic performance is illustrated in Figure 6.

The deterioration on the third rail bending stiffness has a profound effect on the vibrational characteristics of the third rail compared with the deterioration of the supporting structures. It is well known that a flexible beam shows resonance at low frequencies. Besides intense vibration, the aging process and continuous exposure to harsh environmental conditions such as snow, rain, and humidity can expedite the deterioration of the third rail and reduce its structural stiffness. A similar effect can be observed in Figure 6a. The frequencies corresponding to pin-to-pin mode of vibration shifted toward the lower frequency region when the bending stiffness was reduced. However, the pin-to-pin mode of vibration was not affected significantly by the reduced stiffness of supporting structures, as shown in Figure 6b. This is because the pin-to-pin resonance frequency depends on bending stiffness ( $EI$ ) and the span length of the third rail structure [26]. Nonetheless, the

main effect of reducing the stiffness of support structures was observed at approximately 20 Hz. This frequency corresponds to a resonance mode where the entire third rail bounces on the support. This particular mode of resonance is shown in Figure 7. It was observed that, with the deteriorated supporting structures, the overall third rail structure starts resonating at an even lower frequency. Similar resonance modes and characteristics are also reported in railway track dynamics [10].



(a) Change in third rail bending stiffness (EI)



(b) Change in stiffness of the support structure (K)

Figure 6. Effect of structural deterioration on harmonic response of third rail.

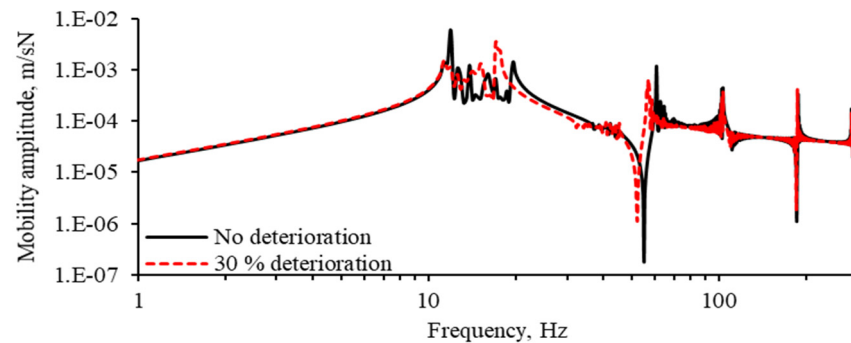


Figure 7. Typical resonance mode (~20 Hz) where whole third rail bounces on support.

#### 4.3.2. Effect of Missing Claws

Another effect of such deterioration in the third rail structure is the failure of the supporting structures. In normal conditions, the third rail is clamped at a certain height above the railway track by the claw structures. Periodic clamping arrangement limits the downward deflection of the third rail due to its self-weight. However, exposure to strong vibration could induce high stress at the claw insulator supports and rail joints, leading to eventual failure of structural components or unfastening of claws [25]. Any broken or

missing claws or supporting components have adverse effect on the dynamic response of the third rail. Furthermore, missing claws increase the sagging of the third rail, which drastically increases the contact force between the rail and the collector shoes. The effects of missing claws or supporting structures on the performance of third rail are discussed in this section.

#### Dynamic Response of the Third Rail with Missing Claws

The most crucial change in the structural parameter due to the damaged or missing claws is the change of the span length. When a single claw structure is broken, the span length between two consecutive support structures becomes double at that particular section, which affects the overall dynamic response of the third rail. For example, a single missing or broken claw structure can be modelled by removing the spring support  $n_1$  in Figure 3. When  $n_1$  is removed, the span length between two consecutive spring supports, i.e.,  $n_0$  and  $n_2$ , becomes  $2*d$ . This change in span length was incorporated in dynamic Equations (7)–(9). Thus, by changing the span length of two consecutive spring supports, the vibration characteristics of the third rail with missing or broken claw structures can be analyzed. The results from both analytical and numerical approaches are shown in Figure 8. The results present a harmonic response in terms of mobility amplitude of the third rail for a single missing claw (*missing claws* =  $n_1$  missing) to three missing claws (*missing claws* :  $n_1$  to  $n_3$ ).

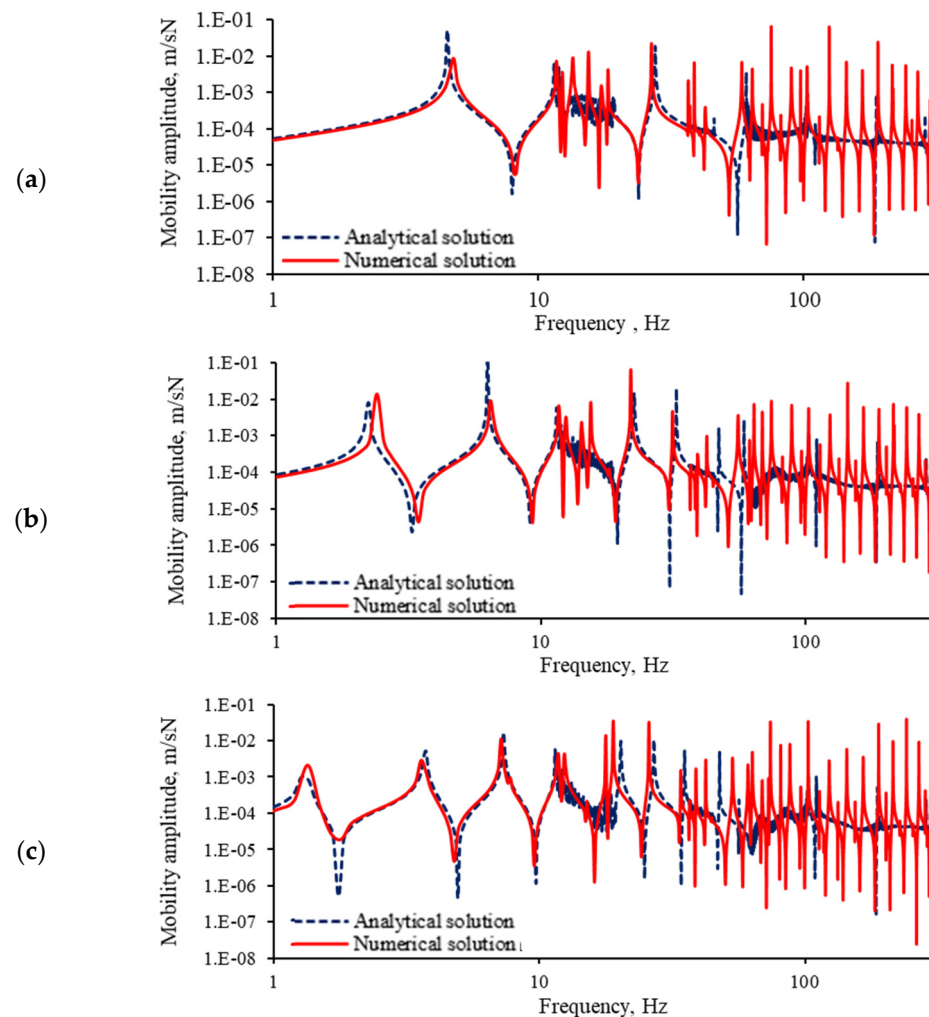


**Figure 8.** Harmonic response of the multi-span third rail with missing claws: (a) number of missing claws = 1; (b) number of missing claws = 2; and (c) number of missing claw = 3.

A damaged supporting component or missing claw resulted in low-frequency resonance below 10 Hz. Furthermore, as the number of missing claws increased, the resonances occurred at even lower frequencies than 10 Hz. Interestingly, the number of resonance that appeared below 10 Hz is equal to the number of missing claws. Moreover, the harmonic responses obtained from both the analytical and numerical approaches are very close to each other. For each number of missing claws, the resonance frequencies are listed in Table 5.

**Table 5.** List of Low-Frequency Resonance below 10 Hz Due to Number of Missing Claws.

No of Missing Claws	Low-Frequency Resonance below 10 Hz Due to Number of Missing Claws					
	1st resonance, Hz		2nd resonance, Hz		3rd resonance, Hz	
	Analytical	Numerical	Analytical	Numerical	Analytical	Numerical
1	4.54	4.8				
2	2.23	2.4	6.19	6.45		
3	1.27	1.35	3	3.6	7.32	7.2

### Sagging of the Third Rail with Missing Claws

Missing claws or supporting components increase the sagging of the third rail and, therefore, exert excessive contact force on the current collector shoes. Excessive contact forces could cause the twisting of the collector shoes, leading to loss of contact with the third rail and interrupting the power supply to the train. The sagging of the third rail and the contact force depends on the number of dropped or missing claws. The deflection of the third rail for a number of missing claws was simulated in ANSYS. The results are presented in Figure 9. With no missing claws, the maximum deflection of the third rail was less than 1.2 mm, which corroborated with the design criteria of the SMRT third rail to limit the third rail deflection below 1.5 mm [28,29] For more than two damaged or missing claw structures, the deflection increased sharply and was found to be about 170 mm in the case of four missing claw structures. Similar results were reported in an investigation conducted by SMRT to inquire the causes of power disruption in train services [28].

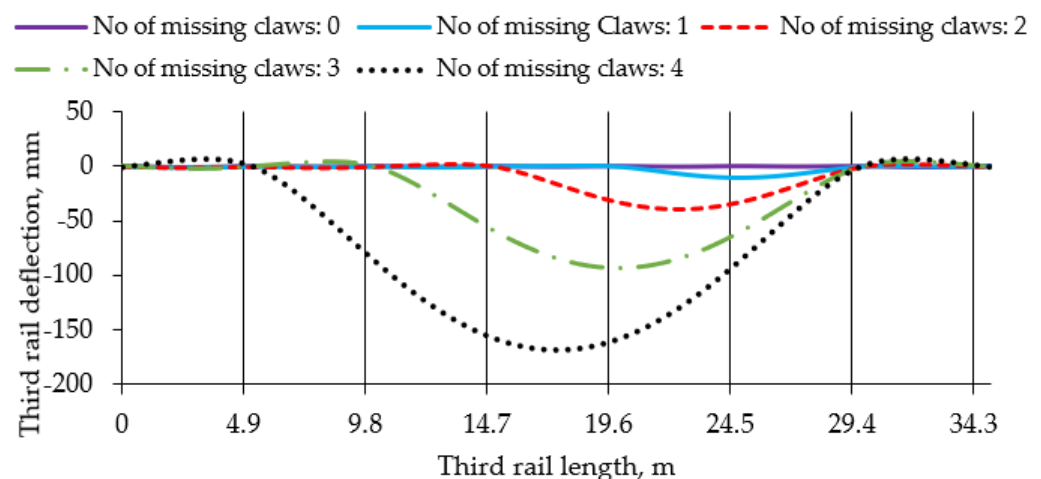


**Figure 9.** Deflection of the third rail due to failure of the support structure.

As expected, the sagging of the third rail increases with the increasing number of missing claws. However, it is interesting to note that the sagging increases much more as the number of missing claws increases. As the contact force on the collector shoes increases with the sagging, more than two missing claws can exert a considerably higher force than normal operating conditions. This will increase the possibility of bottoming out the current collector device’s suspension and damaging the collector shoes. Figure 10 shows the damage and failure of the structural components and current collector shoes because of excessive contact force due to excessive sagging of the third rail.



**Figure 10.** Nature of the damages and structural failures in third rail structure and current collector devices (CCD).

In practice, the third rail alignment can be measured using a linear variable displacement transducer (LVDT), which scans the movement of the collector shoes [30] and gives a rough idea about the sagging of the third rail and possible need for maintenance. The results from Figure 9 can be used to predict the number of missing claws and possible disruption in the operation. Thus, the analysis would help predictive maintenance as the results can be used to detect the possible deterioration or the failure of the structural components.

The current collector device is often modeled as a cantilever arm with a spring and collector shoe attached to it. A simple method to estimate the contact force between the third rail and the collector shoe is to add a constant force ( $F_a$ ) with the force proportional to the spring displacement. The force is applied to ensure proper contact between the collector shoe and the third rail. Similarly, deflection of the third rail increases the displacement of the spring, and the contact force increases. A typical representation of the current collector device and the contact force model is shown in Figure 11a.

A typical value of applied constant force may range from 120 N to 145 N [31]. Assuming the contact shoe is always in contact with the third rail, the displacement of the spring ( $x$ ) can be correlated with the deflection of the third rail ( $u$ ). The total contact force between the collector shoe and the third rail is given by:

$$\text{Contact force}(F_c) = F_a + K_{\text{spring}} * \left(\frac{a}{b}\right)^2 * u \quad (11)$$

Here, the typical values for constant force ( $F_a$ ), spring stiffness ( $K_{\text{spring}}$ ), the distance between the pivot point and spring ( $a$ ), and length of cantilever arm ( $b$ ) are selected to be 120 N, 11300 N/m, 65 mm and 428 mm, respectively [8]. The total contact force considering the deflection of the third rail from Figure 9 was computed for a different number of missing claws. The results are shown in Figure 11b.

Here, it should be noted that the model used for computing the contact force does not consider any structural irregularities such as misalignments, rough surface, and so on. However, this simple model successfully showed that the large deflection of the third rail due to missing claws could exert excessive forces on the current collector devices and cause structural damage.

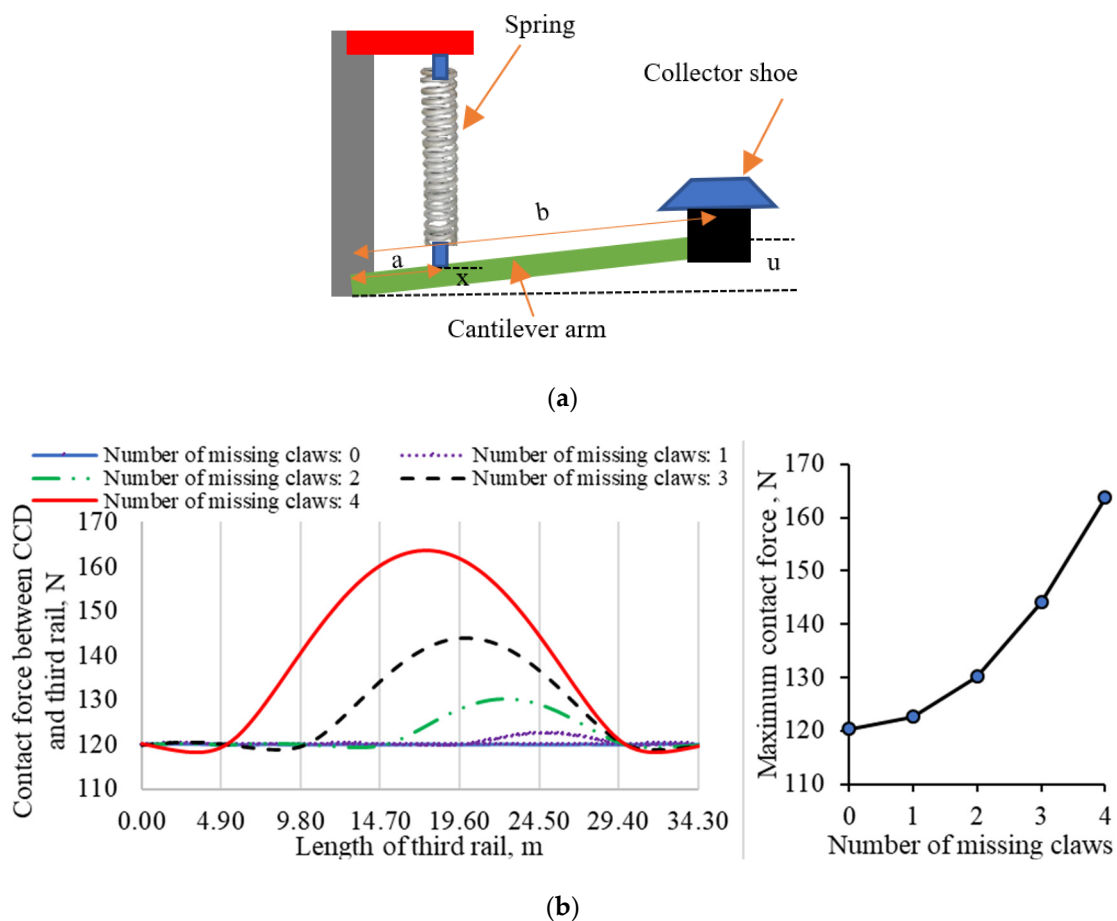


**Figure 11.** (a) Simplified model for current collector device; (b) contact force between collector shoe and third rail due to missing claws.

## 5. Conclusions

The third rail system comprising a long conductor rail and the supporting structures such as brackets, insulators, and claws are modeled to analyze the dynamic performance of the third rail. Using the structural design information and material properties, a 3D Finite Element Model was developed to closely resemble the SMRT third rail system, and numerical analysis was performed using ANSYS simulation. To verify the accuracy of the FEM model, the ANSYS results for single-span third rail were compared with experimental results from the laboratory setup. Thereafter, a multi-span finite element model was developed, and the results were compared with the analytical approach by modeling the third rail as an infinite Euler–Bernoulli beam on periodic spring supports. The modal analysis and harmonic response in terms of mobility analysis were conducted. Furthermore, the analysis was performed to understand the effect of structural failure on third rail vibration characteristics. The study was further extended to include the sagging of the third rail due to structural failure.

The results from both the analytical and FEM analysis approaches showed a good agreement for the pin-to-pin mode of resonance frequencies. The third rail was found to exhibit resonance at a very low frequency starting from 10 Hz. The first five pin-to-pin mode of vibrations were identified below 300 Hz. The analysis showed that structural deterioration decreases the resonance frequencies; as a result, the third rail could exhibit resonance at even low frequencies, below 10 Hz. In fact, the effect of damaged or missing supporting structures such as claws was found to have a more adverse effect on lowering the resonance frequencies. It was found that the third rail with a single missing or damaged claw could occur at a frequency as low as 5 Hz. The resonance frequency reduced

further below 5 Hz with the increased number of consecutive missing or damaged claws. Furthermore, the results suggested that the collector shoe contact force could drastically increase due to the increase in third rail deflection because of the structural failure. The analysis could be further extended to include a moving load exerted by the collector shoe on third rail. Nonetheless, we believe that the current analysis serves as a tool to examine the third rail condition and perform predictive maintenance.

**Author Contributions:** Conceptualization, M.P. and L.J.L.; methodology, M.P., L.J.L. and F.F.Y.; software, M.P. and L.J.L.; validation, M.P. and L.J.L.; formal analysis, M.P.; investigation, M.P.; resources, K.K.; data curation, M.P. and L.J.L.; writing—original draft preparation, M.P.; writing—review and editing, F.F.Y. and K.K.; supervision, F.F.Y.; project administration F.F.Y. and K.K.; funding acquisition, F.F.Y. All authors have read and agreed to the published version of the manuscript.

**Funding:** This research was funded by Singapore Mass Rapid Transit (SMRT), grant number: EIRRA-RP5 and research works were carried out at SMRT-NTU Urban Rail Corporate Laboratory, NTU Singapore.

**Institutional Review Board Statement:** Not applicable.

**Informed Consent Statement:** Not applicable.

**Data Availability Statement:** Not applicable.

**Conflicts of Interest:** The authors declare no conflict of interest.

## References

- Kim, Y.-S.; Jeong, R.-G.; Lee, B.-S.; Park, S.-H.; Lee, W.-D. Development of a Third Rail Type Current Collecting Shoe for the Rubber-Tired AGT System. Available online: [www.Railway-research.org](http://www.Railway-research.org) (accessed on 20 May 2020).
- James, K. *Evaluating the Feasibility of Electrified Rail at the Port of LA/LB*; Metrans: Long Beach, CA, USA, 2011.
- Forman, K. Aluminum/Stainless Steel Conductor Technology: A Case for its Adoption in the US. In Proceedings of the ASME/IEEE Joint Rail Conference, Knoxville, TN, USA, 15–18 April 2013.
- Third Rail. 2015. Available online: <http://www.railsystem.net/third-rail/> (accessed on 20 May 2020).
- Middleton, W.D. Railroad standardization: Notes on third rail electrification. *Railw. Locomot. Hist. Soc. Newsl.* **2007**, *27*, 10–11.
- Hussein, M.F.M. *Vibration from Underground Railways*; University of Cambridge: Cambridge, MA, USA, 2004; Volume 11.
- Monteiro, M. Vibrations Induced by Trains. Case Study: Extension of Track Platform of Gare do Oriente. 2009. Available online: [https://fenix.tecnico.ulisboa.pt/downloadFile/395139464839/Abstract\\_ManuelMonteiro.pdf](https://fenix.tecnico.ulisboa.pt/downloadFile/395139464839/Abstract_ManuelMonteiro.pdf) (accessed on 20 May 2020).
- Jinfa, G.; Jiqin, W.; Yuan, Z. Dynamics analysis of electric shoe and conductor rail system. *J. Vibroeng.* **2014**, *16*, 1992–2007.
- Timoshenko, S. Method of analysis of static and dynamical stresses in rail. In Proceedings of the Second International Congress of Applied Mechanics, Zurich, Switzerland, 12–17 September 1926; pp. 1–12.
- Thompson, D. *Railway Noise and Vibration: Mechanisms, Modelling and Means of Control*; Elsevier: Amsterdam, The Netherlands, 2008.
- Kaewunruen, S.; Remennikov, A. *Dynamic Properties of Railway Track and Its Components: A State-of-the-Art Review*; University of Wollongong: Wollongong, Australia, 2008.
- Yang, X.; Liu, X.; Zhou, S.; Ma, X.; Shen, J.; Zang, J. Vertical random vibration analysis of track-subgrade coupled system in high speed railway with pseudoexcitation method. *Shock Vib.* **2016**, 591–600. [[CrossRef](#)]
- Bhargava, B. Railway electrification systems and configurations. In Proceedings of the 1999 IEEE Power Engineering Society Summer Meeting, Edmonton, AB, Canada, 18–22 July 1999.
- Vera, C.; Suarez, B.; Paulin, J.; Rodriguez, P. Simulation model for the study of overhead rail current collector systems dynamics, focused on the design of a new conductor rail. *Veh. Syst. Dyn.* **2006**, *44*, 595–614. [[CrossRef](#)]
- Paulin, J.; Sanz, J.D.; Vera, C. Development of a new high-performance overhead conductor rail using simulation models, and their validation through field testing. In Proceedings of the 7th WCRR, Montreal, QC, Canada, 4–8 June 2006.
- Weston, P.; Stewart, E.; Roberts, C.; Hillmans, S. Analysis of electric shoe gear dynamics. In Proceedings of the 8th World Congress on Railway Research, Seoul, Korea, 18–22 May 2008.
- Longqi, W.; Tjhen, L.S.; Yao, Z. Detection of loose fasteners in a third rail support assembly using a wavelet analysis. *IES J. Part A Civ. Struct. Eng.* **2014**, *7*, 73–82. [[CrossRef](#)]
- Zhang, X.; Thompson, D.; Sheng, X. Differences between Euler-Bernoulli and Timoshenko beam formulations for calculating the effects of moving loads on a periodically supported beam. *J. Sound Vib.* **2020**, *481*, 115432. [[CrossRef](#)]
- Gramoll, K. *Multimedia Engineering Mechanics of Materials*, University of Oklahoma. 2017. Available online: <https://ecourses.ou.edu/cgi-bin/ebook.cgi?doc=&topic=me> (accessed on 20 May 2020).
- Døssing, O. *Structural Testing: Mechanical Mobility Measurements*; Brüel & Kjær: Nærum, Denmark, 1988.
- DataPhysics. SignalCalc Software. Available online: <https://www.dataphysics.com/> (accessed on 12 March 2020).

22. MEScopeVES. Available online: <https://www.vibetech.com/solutions/visual/> (accessed on 12 March 2020).
23. Avitabile, P. Could You Please Explain the Basic Steps to Acquire Data for Modal Testing. In *Modal Space—In Our Own Little World*; Brüel & Kjær: Nærum, Denmark, 2002.
24. Avitabile, P. I Still Don't Understand Curvefitting... How Do You Get Mode Shapes from FRFs. In *Modal Space—In Our Own Little World*; Brüel & Kjær: Nærum, Denmark, 1999.
25. Avitabile, P. Curvefitting Is So Confusing to Me! What Do All the Different Techniques Mean. In *Modal Space—In Our Own Little World*; Brüel & Kjær: Nærum, Denmark, 1999.
26. De Man, A. Pin-Pin Resonance as a Reference in Determining Ballasted Railway Track Vibration Behaviour. *Heron Engl. Ed.* **2000**, *45*, 35–52.
27. Fan, W.; Qiao, P. Vibration-based Damage Identification Methods: A Review and Comparative Study. *Struct. Health Monit.* **2011**, *10*, 83–111. [[CrossRef](#)]
28. Singapore Mass Rapid Transit (SMRT). *Report of the Committee of Inquiry into the Disruption of MRT Train Services on 15 and 17 December 2011, Annex A*; Singapore Mass Rapid Transit (SMRT): Singapore, 2012.
29. Singapore Mass Rapid Transit (SMRT). *Report of the Committee of Inquiry into the Disruption of MRT Train Services on 15 and 17 December 2011, Annex B*; Singapore Mass Rapid Transit (SMRT): Singapore, 2012.
30. SMRT Third Rail Maintenance to Prevent Disruptions. 2016. Available online: <http://blog.smrt.com.sg/smrt-third-rail-maintenance-to-prevent-disruptions/> (accessed on 11 April 2020).
31. Stemann-Techni. TRSG Bottom-Running-System. Available online: [http://stemmann.com/en/products/3rd\\_rail\\_current\\_collector/trsg\\_bottom\\_running\\_system](http://stemmann.com/en/products/3rd_rail_current_collector/trsg_bottom_running_system) (accessed on 1 July 2020).